1

2

3

4

5

6

Cell shape independent FtsZ dynamics in synthetically remodeled cells

Short title: FtsZ dynamics in shapes

Bill Söderström[1*$], Alexander Badrutdinov[2],
Helena Chan[1], and Ulf Skoglund[1]

[1]Structural Cellular Biology Unit
[2] Mechanical Engineering and Microfabrication Support Section
Okinawa Institute of Science and Technology, 904-0495 Okinawa, Japan

* Address correspondence to:
Mail Bill.soederstroem@oist.jp or soderstrombill@gmail.com,
Tel: +81 080-6483-7515, Fax : +81 098-982-3420
[$] Twitter: @BillSoderstrom

Key words: FtsZ, Micron pillars, STED, Z-square, Z-heart

Abstract

The FtsZ protein is a key regulator of bacterial cell division. It has been implicated in acting as a scaffolding protein for other division proteins, being a force generator during constriction, and more recently, as an active regulator of septal cell wall production. During an early stage of the division cycle, FtsZ assembles into a heterogeneous structure coined the "Z-ring" due to its resemblance to a ring confined by the midcell geometry. While *in vitro* experiments on supported lipid bilayers have shown that purified FtsZ can self-organize into a swirling ring roughly the diameter of a bacterial cell, it is not known how, and if, membrane curvature affects FtsZ assembly and dynamics *in vivo*.

To establish a framework for examining geometrical influences on proper Z-ring assembly and dynamics, we sculptured *Escherichia coli* cells into unnatural shapes, such as squares and hearts, using division- and cell wall-specific inhibitors in a micro fabrication scheme. This approach allowed us to examine FtsZ behavior in engineered "Z-squares" and "Z-hearts", and in giant cells up to 50 times their normal volume. Quantification of super-resolution STimulated Emission Depletion (STED) nanoscopy data showed that FtsZ densities in sculptured cells maintained the same dimensions as their wild-type counterparts. Additionally, time-resolved fluorescence measurements revealed that FtsZ dynamics were generally conserved in a wide range of cell shapes. Based on our results, we conclude that the underlying membrane environment is not a deciding factor for FtsZ filament maintenance and treadmilling *in vivo*.

Introduction

Most bacterial cells divide by binary fission, whereby one mother cell splits into two identical daughters [1-3]. Decades of study have led to a detailed understanding of how the cell division machinery, the divisome, carries out this task during the later stages of the cell cycle [4,5]. At the heart of this process is the eukaryotic tubulin homologue, FtsZ [6] that, together with its membrane anchors ZipA and FtsA, forms an intermediate structure called the proto-ring (Fig. 1a) [7]. Functioning as a recruitment base, the proto-ring components then enlist the remaining essential division proteins to form a mature 'divisome' [5]. As soon as it is fully assembled, the divisome starts to constrict the cell envelope by reshaping the septal geometry, ultimately leading to sequential closure of the inner and outer membranes [8-10].

In rod-shaped model bacteria such as *Escherichia coli* and *Bacillus subtilis*, FtsZ is believed to organize into short bundles of filaments, roughly 100 nm in length [11,12], that treadmill at the septum with a circumferential velocity in the order of 20-30 nm/s [13-15]. The treadmilling filaments guide and regulate septal peptidoglycan (PG-) production and ingrowth, leading up to septation [16]. This mode of action may be limited to rod-shaped bacteria that have two separate PG-machineries, as opposed to cocci, which have only one PG-machinery that is capable of finalizing division in cells with inhibited FtsZ dynamics [17].

At a late stage of membrane constriction, but prior to inner membrane fusion, FtsZ disassembles from midcell, indicating the possible existence of an upper limit of ring curvature [6,9]. However, other geometrical constraints that might govern Z-ring maintenance and stability are currently unclear. We were curious as to whether geometrical changes to cell shape would influence Z-ring formation and dynamics. In

3

93   this study, we examined FtsZ formation, organization and behavior in *E. coli* cells that

94   were sculptured into complex geometrical shapes in micron sized holes.

95

96   **Results**

97   *FtsZ structure and dynamics in Z-rings are not sensitive to increased ring size*

98   As a reference for unmodified division rings, we imaged Z-rings in *E. coli* cells

99   expressing FtsZ-mNeonGreen as the only source of FtsZ [18]. Under our experimental

100   conditions, this strain produced normal-looking, sharp Z-rings (Supplementary Fig. S1)

101   and grew and divided similarly to wild-type (WT) *E. coli* (MC4100) (Supplementary Fig.

102   S2a-e). We then trapped the cells in a vertical position in micron-sized holes that were

103   produced in agarose pads using silica micron pillar arrays [14] (Fig. 1b, Supplementary

104   Fig. S3), and imaged the cells using super-resolution time-gated Stimulated Emission

105   Depletion (gSTED) nanoscopy. In these standing cells, a heterogeneous Z-ring with

106   distinct FtsZ-mNeonGreen densities was clearly seen traversing the circumference of

107   the cell (Fig. 1c), similar to what has been observed before [12,14].

108   Previous work has shown that FtsZ densities generally maintain the same length

109   throughout envelope constriction [12,14]. We wanted to see if this was also true for cells

110   growing in the opposite direction, *i.e.* would FtsZ densities maintain the same

111   dimensions in Z-rings of cells with increased diameter at midcell? In order to increase

112   cell diameter, we treated *E. coli* cells with A22 and cephalexin (hereafter collectively

113   referred to as 'drugs'), in a way similar to what has previously proven successful for

114   cell shape manipulations [19]. A22 disrupts MreB dynamics and therefore perturbs the

115   characteristic rod-shape of *E. coli* cells [20,21], while cephalexin blocks cell division by

116   inhibiting the transpeptidase activity of FtsI [22]. The net effect of this dual drug treatment

4

117   is the growth of cells into shapeable blebs that are unable to divide (Supplementary

118   Fig. S4a).

119   As long as cell width remains less than cell length, FtsZ molecules should be directed

120   to midcell by the Min system [19], such that a ring-like structure should be observed in

121   the xy-plane of vertically-oriented, standing cells (Fig. 1b). To confirm this, we exposed

122   *E. coli* cells expressing FtsZ-mNeonGreen to drugs, and then trapped the cells

123   vertically in holes with a depth of 4.5 - 6 μm, and a diameter of up to 3.5 μm. Depending

124   on the size of the holes, cells were incubated between 120 and 240 minutes prior to

125   imaging; over-incubation resulted in cells that outgrew the holes (Supplementary Fig.

126   S4b. Letting cells grow for long time (> 10 h) produced giant blobs with internalized

127   FtsZ-mNeonGreen chain, see SI Text). We found "normal-looking" Z-rings that

128   spanned the midcell circumference for the entire range of cell diameters that were

129   imaged (~ 1 - 3 μm) (Fig. 1d-e). Importantly, confocal Z-stacks showed that each cell

130   contained only one Z-ring (Supplementary Fig. S5 and Movie SM1). Close inspection

131   of STED images revealed that the Z-rings in larger cells were composed of fluorescent

132   densities (Fig. 1f) with average lengths and widths of 132 ± 48 nm and 88 ± 9 (n =

133   172), respectively, which were similar (p > 0.05) to Z-ring densities in untreated cells

134   (Fig. 1g).

135   After we had established that large Z-rings can form in cells with increased diameter,

136   we proceeded to calculate FtsZ dynamics in these larger rings. However, strains

137   expressing FtsZ-FP as the only source of FtsZ have been shown to have a phenotype

138   similar to that of FtsZ mutants deficient in GTPase activity, with severely impaired

139   treadmilling speed [13]. Therefore, we chose to image cells that expressed FtsZ-GFP

140   from an ectopic locus on the chromosome, in addition to native FtsZ [23]. Earlier studies

141   showed that FtsZ-GFP, when expressed at levels below 50 % of total cellular FtsZ

142 levels, caused no observable phenotypic changes [9,12,23,24]. In our experimental setup,

143 FtsZ-GFP was expressed at ~ 30 % of total FtsZ levels (Supplementary Fig. S2).

144 Structured Illumination Microscopy (SIM) of drug-treated *E. coli* cells expressing FtsZ-

145 GFP showed large heterogeneous rings that were similar to those of FtsZ-

146 mNeonGreen (Fig. 1h - k). Time-lapse images revealed that FtsZ densities moved

147 around the midcell circumference, even in Z-rings with a diameter up to three times

148 larger than that of a WT cell (Supplementary Movie SM2). There was no difference in

149 the speed of individual densities in the rings of untreated cells compared to those in

150 sculptured cells that had a diameter 50 - 200 % larger than WT (26 ± 15 nm/s and 30

151 ± 18 nm/s, respectively) (Fig. 1l - m), suggesting that filament treadmilling speed is not

152 influenced by the length of the cell circumference. ZipA-GFP, an FtsZ membrane

153 anchor, also moved at essentially the same speed in both normal- and large-sized

154 rings (26 ± 8 nm/s) (Supplementary Fig. S6 and Movie SM3), which is comparable to

155 previously reported speeds [14].

156 Since treadmilling behavior of FtsZ in large cells was very similar to that in WT cells,

157 we were curious to see whether FtsZ subunit exchange in the rings would also be

158 similar. To assess this, we performed Fluorescence Recovery After Photobleaching

159 (FRAP) experiments on both untreated and drug-treated cells. We bleached half of

160 the FtsZ-GFP molecules in the rings of standing cells and monitored fluorescence

161 recovery over time (Fig. 2a). Z-rings in untreated cells had a mean $t_{1/2}$ recovery time

162 of 8.4 ± 1.9 sec, n = 23 (Fig. 2b), consistent with previous studies [14,25]. Surprisingly,

163 the average $t_{1/2}$ recovery time was the same for Z-rings with a wide range of diameters

164 (Fig. 2b). We believe this reflects the formation of a greater number of FtsZ filaments

165 at the inner membrane of expanded cells, due to larger accessible surface area (Fig.

166 2c), while filament treadmilling speed remains unchanged.

167

168 *The 'FtsZ-square'*

169 Next, we wanted to know if drug-treated cells placed in deep (5 μm) rectangular

170 volumes would adapt to these shapes and effectively form 'Z-rectangles' or 'Z-

171 squares' instead of 'Z-rings'. Previous work has shown that cells can adapt to

172 rectangular shapes in shallow wells, approximately 1 μm deep [19]. Here, we produced

173 quadrilateral patterns in agarose pads using silica micron pillar arrays similar to those

174 previously described [14], with the exception that the pillars were rectangular and 5.5 $\pm$

175 0.5 μm in height. Side lengths of the micron chambers were up to 3.5 μm in length

176 (Supplementary Fig. S7), resulting in well volumes up to 80 μm^3, roughly 50-fold larger

177 than the volume of a WT cell (assuming a WT cell size of 2 μm in length and 1 μm in

178 width) (Supplementary Fig. S8).

179 Drug-exposed cells expressing FtsZ-mNeonGreen were placed in rectangular micron

180 holes and incubated at room temperature for 300 - 420 minutes (longer incubation

181 times were needed due to increased well size). The cells adapted to their new shapes

182 and formed rectangular cuboids with only one "Z-square" per cell (Fig. 3a,

183 Supplementary Movie SM4). Notably, FtsZ densities were observed both in the sharp

184 corners and along the sides of the rectangles (Fig. 3b, Supplementary Fig. S9).

185 Quantification of the FtsZ-mNeonGreen densities showed that they had similar

186 dimensions to those in untreated cells, with an average length of 105.4 $\pm$ 39.6 nm and

187 width of 79.6 $\pm$ 18.2 nm (n = 147) (Fig. 3c). This suggests that FtsZ filament

188 dimensions *in vivo* are insensitive to membrane curvature (or lack thereof).

189 To generate a fluorescent FtsZ fusion protein that could be used for both super-

190 resolution STED imaging and examination of filament dynamics when grown in rich

191 media at 37 °C, we constructed a plasmid-expressed FtsZ-mCitrine fusion. FtsZ-

7

192 mCitrine was expressed from an IPTG-inducible, medium copy-number plasmid,

193 pTrc99a, at a level approximately equal to 30 % of total cellular FtsZ. Under these

194 conditions, FtsZ-mCitrine formed normal-looking, sharp Z-rings (Supplementary Figs.

195 S1 and S2). Cells expressing FtsZ-mCitrine were then exposed to drugs, trapped in

196 rectangular micron-sized holes, and incubated for 180 - 280 minutes at room

197 temperature before gSTED imaging. We found that FtsZ-mCitrine formed filaments

198 that were 118.3 $\pm$ 41.3 nm long and 86.3 $\pm$ 22.5 nm wide (n = 162), similar to FtsZ-

199 mNeonGreen filament dimensions (Fig. 3c, Supplementary Fig. S10), indicating that

200 fluorophore choice did not influence cluster dimensions in the rings. For consistency,

201 we also imaged rectangular cells expressing FtsZ-GFP from the chromosome using

202 SIM (Supplementary Fig. S10). All three strains tested adapted to the rectangular

203 shape, producing sharped-cornered "Z-rectangles".

204

205 *FtsZ dynamics in rectangular-shaped cells*

206 In order to examine the dynamics of FtsZ in rectangular cells, we performed time-lapse

207 imaging on cells expressing either FtsZ-mCitrine or FtsZ-GFP. Although a few

208 fluorescence spots were abnormally bright and immobile (~ 1 spot / 5 cells, with a

209 maximum of 2 spots in one cell) (Fig. 4b, Supplementary Movie SM7. Red arrow), the

210 majority of FtsZ densities were highly dynamic (Fig. 4a-b, Supplementary Movies SM5

211 - SM6). Note that the bright, immobile spots were excluded from treadmilling analyses.

212 Close inspection of time-lapse sequences suggested that FtsZ bundles in rectangular-

213 shaped cells may be able to treadmill, even in right-angled corners (Fig. 4b-c,

214 Supplementary Movie SM8). The average speed of FtsZ-mCitrine densities in

215 rectangular cells with perimeter lengths up to 13 μm (more than four times the

216 circumference of a WT cell) was 27.6 $\pm$ 12.5 nm/s (n = 109), which was consistent with

217   the measured treadmilling speed of FtsZ-GFP in rectangular cells (25.3 ± 11.3 nm/s,

218   n = 122) (Fig. 4d), large cylindrical cells (30 ± 18 nm/s, Fig. 1m) and untreated cells (~

219   25 nm/s) [13,14].

220   To determine whether the dynamics of FtsZ subunit exchange are affected by changes

221   to circumferential length and shape, we collected FRAP measurements on FtsZ

222   bundles in rectangular-shaped cells (Fig. 4e, Supplementary Movie SM9). The

223   recovery times of half-bleached rectangles of varying sizes matched those of rings,

224   with mean $t_{1/2}$ recovery times of 9.85 ± 2.58 s (n = 24) and 9.15 ± 2.55 s (n = 22) for

225   FtsZ-mCitrine and FtsZ-GFP, respectively (Fig. 4f). This suggests that subunit

226   exchange from the cytoplasmic FtsZ pool is independent of circumference length and

227   membrane curvature. The data thus far indicate that the maintenance and dynamics

228   of FtsZ filaments are preserved in both large Z-rings and Z-rectangles of varying size.

229

230   *FtsZ dimensions and dynamics in heart-shaped cells*

231   To examine whether FtsZ could literally be (at) the heart of cell division, we engineered

232   micron pillar arrays that were heart-shaped (Supplementary Fig. S11). Heart shapes

233   were chosen because they would sculpt cells in such a way that highly curved, straight,

234   and angled membrane segments would be present within a single cell. Drug-treated

235   *E. coli* cells expressing cytoplasmic GFP, FtsZ-mNeonGreen or FtsZ-mCitrine were

236   sculptured into hearts as described above (Fig. 5a). Perhaps not surprisingly,

237   quantification of 155 individual FtsZ densities from the heart-shaped cells revealed

238   dimensions similar to those in round and rectangular cells (129 ± 44 nm long and 84

239   ± 9 nm wide) (Fig. 5b). We also found that the average speed of FtsZ-mCitrine in heart-

240   shaped cells (22 ± 10 nm/s, n = 44) was essentially the same as that in untreated cells

241   (Figure 5c, Supplementary Movie SM10).

9

242   For about one-third of the heart-shaped cells, we noticed bright spots of internalized

243   FtsZ-FP signal that accumulated close to the cell center (Figure 5c, green arrowhead).

244   Although we couldn't distinguish whether these were true FtsZ clusters or aggregated

245   protein, cytoplasmic clustering of FtsZ in WT cells have previously been reported [12].

246   Furthermore, although most hearts had FtsZ-FP signal spanning the full perimeter of

247   the cell, approximately 20 % were only "half full" (Fig. 5d, left). We do not fully

248   understand the underlying reason for this, however it is unlikely due to image focus or

249   cell tilt issues, as every cell was scanned in the z direction prior to imaging.

250   Nevertheless, when we subjected the heart-shaped cells to FRAP, fluorescence

251   recovery rates were equal for both full and half-full hearts (Fig. 5d), with mean $t_{1/2}$

252   recovery times of 7.1 ± 1.1 s (n = 24) and 6.9 ± 0.9 s (n = 9), respectively (Fig. 5e).

253

254   *FtsZ-"rings" form in complex cell shapes*

255   To explore if cell geometry plays a role in Z-"ring" formation, we set out to remodel

256   cells into other complex shapes. Even though highly complex-shaped bacteria occur

257   in nature, such as star-shaped bacteria [26], we wanted to test whether rod-shaped *E.*

258   *coli* cells would allow themselves to be drastically remodeled. Using micron pillars of

259   various shapes, we produced holes in agarose pads such that drug-exposed cells

260   could be sculptured into complex shapes, such as pentagons, half-moons, stars,

261   triangles and crosses (Fig. 6a, middle row. Supplementary Fig. S11). The cells

262   conformed remarkably well to these shapes, forming sharp boundary angles < 70°

263   (Fig. 6a, Star). After we confirmed that cells could adapt to these complex shapes, we

264   placed cells expressing FtsZ-mCitrine into the micron holes, allowed for reshaping to

265   occur, and then imaged the cells using STED nanoscopy. Cells of all tested shapes

266   produced easily recognizable FtsZ-"shapes" at midcell (Fig. 6a, bottom row).

10

267   Subsequent analysis of the lengths and widths of the FtsZ densities revealed little

268   difference in dimensions between the different shapes, suggesting a minimal role of

269   cell shape in determining FtsZ cluster dimensions *in vivo* (Fig. 6b). Additionally, time-

270   lapse imaging of cells expressing FtsZ-mCitrine in various shapes showed similar

271   dynamics to those measured in untreated cells (Supplementary Movie SM10).

272

273   **Conclusions**

274   Cells, both bacterial and eukaryotic, have the ability to adapt remarkably well to their

275   local environments [27-31], reverting to their original shapes after stress [32,33] and dividing

276   with striking midcell accuracy even when remodeled into irregular cell shapes [27,30]. In

277   bacteria, the tubulin homologue FtsZ assembles into a ring-like structure at midcell

278   and is responsible for overall maintenance of the cell division machinery [5,6]. The

279   general dynamics and organization of the FtsZ-ring have been shown to be quite

280   similar across many bacterial species [11,13-15,17,34-37]. Common to these species is

281   confinement of the FtsZ-ring to a circular geometry at midcell. Strikingly, when purified

282   FtsZ (together with its membrane anchor FtsA) is placed on supported lipid bilayers, it

283   assembles into a dynamic, swirling ring-like assembly with a diameter resembling that

284   of wild-type *E. coli* cells (approximately 1 μm), hinting at an intrinsically preferred FtsZ-

285   ring curvature [6,38].

286   In this study, we characterized FtsZ midcell accumulation and dynamics in cell shape-

287   determining environments by 'looking through the Z-ring' along the long-axis of cells.

288   We observed normal-looking FtsZ-rings in cells with diameters three times the size

289   found in WT cells. However, this might not be surprising, considering only ~ 30 % of

290   the pool of FtsZ molecules are in the ring of WT cells at any given point in time [39].

291   Quantification of FtsZ dimensions revealed little variation between different cell

11

292   shapes, such as squares, pentagons, triangles and stars (on average 123 x 80 nm,

293   length x width, respectively, and summarized in Table 1), suggesting that local

294   membrane geometry has minimal influence on FtsZ cluster dimensions. Compared to

295   untreated cells, rectangular and heart-shaped cells with perimeter lengths more than

296   four times that of a WT cell exhibited similar overall dynamics of FtsZ, as FtsZ-FP

297   fluorescence densities treadmilled at the same average velocity and FtsZ subunit

298   exchange occurred at similar rates (Table 2), independent of cell shape and size.

299

300   In summary, our results from different shaped cells show that Z-"ring" formation and

301   dynamics are not limited to cells of a certain shape or size. This agrees with previous

302   findings, which show that internal cellular structures are maintained in cells that have

303   been reshaped into unnatural forms [19]. Our observation that FtsZ clusters conform to

304   the geometric shape of the membrane at midcell suggests that FtsZ-ring formation is

305   not affected by changes in membrane curvature. Indeed, cell shape and size are

306   important for proper cellular functions [40], however, with the many naturally-occurring

307   shape variations of bacteria [26,41], it is perhaps not surprising that FtsZ can adapt to

308   changing environments without compromising its own ability to maintain fundamental

309   functionality. Although our data do not explicitly show that sculptured cells can divide

310   (since downstream division proteins were inhibited), the fact that the dynamic

311   properties of FtsZ are conserved suggests that this may be possible. One particular

312   implication of this is the notion that the Z-ring can be decoupled from the division

313   process but with maintained dynamics, making treadmilling a possible requirement for

314   divisome assembly and organization in rod shaped model bacteria, as previously

315   suggested for cocci [17]. Presently, we have shown *in vivo* that *E. coli* FtsZ-ring

316   formation and dynamics are conserved, irrespective of cell shape and size.

12

Methods

Bacterial growth

Pre-cultures were grown overnight in 20 ml of rich media (LB) at 37 °C or M9 minimal media supplemented with 1μg ml^{-1} thiamine, 0.2 % (w/v) glucose and 0.1 % (w/v) casamino acids. The following morning, cultures were back-diluted 1:50 in either LB or M9 (with supplements) and antibiotics (ampicillin 25 μg ml^{-1}) when needed, and incubated at 30 °C or 37 °C.

Fluorescent protein production

Chromosomally-encoded FtsZ-mNeonGreen was integrated at the native *ftsZ* locus and did not require any inducer [18]. Chromosomally-encoded FtsZ-GFP (strain BS001), GFP^{CYTO} (strain BS008) and ZipA-GFP were induced with 2.5 μM, 5 μM and 50 μM IPTG, respectively [9].

The plasmid pHC054 (*ftsZ-mCitrine*) was constructed using Gibson assembly [42] to generate an IPTG-inducible FtsZ-mCitrine fusion expressed from pTrc99a [43]. PCR was performed using Q5 High-Fidelity DNA polymerase (New England Biolabs). A DNA fragment containing *ftsZ* was amplified from *E. coli* MC4100 genomic DNA using primers FtsZ(F) (5'-caatttcacacaggaaacagaccatggatgtttgaaccaatggaac-3') and FtsZ(R) (5'-gcccttgctcaccatctgcaggttgttgttatcagcttgcttacgcagg-3'). *mCitrine* was amplified from mCitrine-N1 plasmid DNA using primers mCitrine(F) (5'-cgtaagcaagctgataacaacaacctgcagatggtgagcaagggcgaggag-3') and mCitrine(R) (5'-ccgccaaaacagccaagctttacttgtacagctcgtccatgc-3). pTrc99a plasmid DNA was amplified using primers pTrc99a(F) (5'-ccatggtctgtttcctgtgtg-3') and pTrc99a(R) (5'-aagcttggctgttttggcgg-3'). The *ftsZ* and *mCitrine* coding regions are separated by a short linker encoding NNNLQ. The plasmid sequence was verified by DNA sequencing

13

342   (Fasmac, Japan). FtsZ-mCitrine expression was induced with 2.5 µM IPTG. All FtsZ

343   levels were quantified using Western blotting.

344

345   *Western blot analysis*

346   Cell extracts from a volume corresponding to 0.1 OD_{600} units were collected for each

347   strain to be analyzed. The extracts were suspended in loading buffer and resolved by

348   SDS-PAGE gel electrophoresis. Proteins were transferred to nitrocellulose

349   membranes using a semi-dry Transfer-Blot apparatus (Bio-Rad). The membranes

350   were blocked in 5 %(w/v) milk and probed with antisera to FtsZ (Agrisera, Sweden)

351   and detected using standard methods.

352

353   *Nanofabrication of micro arrays*

354   Micron pillars were engineered using two different, but related, approaches. The first

355   approach was used for round and square/rectangular micron pillars, and was adapted

356   from [14,15]. Briefly, using a multi-step process similar to that described in [44], micron-

357   scale pillars were fabricated on a silicon (Si) substrate by reactive ion etching. A

358   pattern of hard-baked photoresist was created on a Si surface using UV lithography,

359   to work as a mask for etching. Subsequent etching was performed using an Oxford

360   Plasmalab100 ICP180 CVD/Etch system, with a mixture of SF_6 and O_2 plasma as an

361   etchant. For our process, a SF_6:O_2 ratio of 1:1 was optimal. After etching, the

362   remaining photoresist was removed by O_2 plasma treatment. Pillar arrays (1 x 1 cm or

363   2 x 2 cm) with round pillars were engineered to contain one micron-sized pillar every

364   5 µm, with dimensions between 0.9 and 3.5 µm wide and 5.25 $\pm$ 0.75 µm high

365   (Supplementary Fig. S3). Pillar arrays (1 x 1 cm) with square pillars contained micron-

366   sized pillars approximately every 5 μm, with side lengths varying between 1.8 and 3.5

367   μm, and heights of 5.5 ± 0.5 μm (Supplementary Fig. S7).

368   To create more complex shapes, a second approach, based on electron beam

369   lithography was used. For this, the micron-scale structures were fabricated on a Si

370   substrate by a multi-step process, which was a combination of electron beam

371   lithography and reactive ion etching techniques. Similar approaches to silicon

372   patterning are described in a number of earlier works [44-47]. First, a pattern of e-beam

373   resist was created on a Si surface using e-beam lithography. A 50 nm-thick Ti layer

374   was then deposited, and a lift-off process was used to create a metal mask for etching.

375   The use of a metal mask, instead of a baked e-beam resist mask, was necessary due

376   to the high selectivity ratio required for generating structures only a few microns in

377   height. Finally, the etching process was performed as described above, using an

378   Oxford Plasmalab100 ICP180 CVD/Etch system and a mixture of SF_6 and O_2 plasma

379   as an etchant. For our process, a $SF6:O_2$ flow ratio of 3:2 produced the best results,

380   with a Si:Ti etching selectivity ratio of approximately 100:1. Increased concentration of

381   O_2 in the mixture has two effects: (i) it improves etching anisotropy, which is essential

382   for avoiding shape distortion from the undercut effect, and (ii) it reduces the selectivity

383   ratio, as the Si etch rate gets slower. After etching, the structures were characterized

384   using a Dektak surface profiler and SEM imaging. The micron structure arrays, which

385   contained various shapes (hearts, triangles, pentagons, half-moons and crosses),

386   were fabricated on 1 x 1 cm Si chips with inter-structure distances of approximately 5

387   μm, and structure heights of 5.5 ± 0.5 μm (Supplementary Fig. S11).

388

389

390

15

Micron-sized chamber production and cell growth

Liquefied agarose (5% w/v) in M9 minimal media (supplemented with 0.2 % glucose, 0.1 % casamino acids, 2 µg ml^{-1} thiamine, 40 µM A22 and 20 µg ml^{-1} cephalexin) was dispersed on glass slides and the silica mold (pillar facing downwards) was placed on top. The molds contained either round or rectangular pillars, or various geometrical shapes, as described above. Once the agarose solidified, the mold was removed and ~ 5 µl of live cell culture at OD$_{600}$ 0.4 - 0.55 (pre-treated with 16 µM A22 for 10 - 15 minutes) was applied on top. To allow the cells to adapt to the different shapes, slides were incubated at RT or 30 °C in a parafilm-sealed petri dish together with a wet tissue to prevent drying. After incubation, cells were covered with a pre-cleaned cover glass (♯1.5) for live cell imaging. For STED imaging, cells were first fixed with ice-cold methanol for 5 minutes and carefully rinsed with PBS prior to cover glass application.

Microscopy

Gated STED (gSTED) images were acquired on a Leica TCS SP8 STED 3X system, using a HC PL Apo 100x oil immersion objective with NA 1.40. Fluorophores were excited using a white excitation laser operated at 488 nm for mNeonGreen and 509 nm for mCitrine. A STED depletion laser line was operated at 592 nm, using a detection time-delay of 0.8 – 1.6 ns for both fluorophores. The total depletion laser intensity was in the order of 20 - 40 MW/cm^2 for all STED imaging. The final pixel size was 13 nm and scanning speed was either 400 or 600 Hz. The pinhole size was set to 0.9 AU.

Epi-fluorescence and confocal images were acquired on either a Zeiss LSM780 or Zeiss ELYRA PS1 (both equipped with a 100X 1.46NA plan Apo oil immersion objective) with acquisition times between 0.3 and 2 sec. Time-lapse series for

16

416   generating kymographs were recorded at 2 sec intervals for a time period of at least

417   118 sec.

418   SIM images were acquired using a Zeiss ELYRA PS1 equipped with a pco.edge

419   sCMOS camera. The final pixel size in SIM images was 24 nm. Individual images were

420   acquired using an acquisition time of 200 ms per image (a total of 15 images were

421   acquired per SIM image reconstruction) and subsequently reconstructed from the raw

422   data using ZEN2012 software. SIM time-lapse movies (containing at least 14 frames)

423   were recorded without time delays between image stacks.

424   Confocal Z-stacks (focal plane $\pm$ ~ 3.5 µm) were acquired on a Leica TCS SP8 STED

425   3X system (operated in confocal mode) using predetermined optimal system settings

426   (Leica, LAS X), with 0.22 µm steps (resulting in 30-32 images per stack), and pinhole

427   size 1 AU. All imaging was performed at RT (~ 23-24 °C).

428

429   *FRAP measurements*

430   Confocal FRAP measurements were performed on a Zeiss LSM780 system using a

431   100x 1.4 NA plan Apo oil immersion objective and pinhole size 60 µm, as described

432   [14]. Bleaching was performed for 0.5-0.7 s using 100% laser power applied over the

433   region of interest. Data were collected in time intervals of 1 - 2 sec until steady state

434   was reached. Following background correction, and to account for overall successive

435   bleaching, the fluorescence intensity (F) of the bleached region (half a ring) was

436   normalized to the average ring fluorescence of an unbleached area of the same size,

437   for each time point (t); $F_{NORM}(t) = F_{BLEACHED}(t)/(F_{BLEACHED}(t)+ _{UNBLEACHED}(t))$. All data

438   were exported to Origin9 Pro and data points were fitted to the single exponential

439   function $F(t) = F_{end} - (F_{end} - F_{start})* e^{-kt}$, where F(t) is the fluorescence intensity at time

440   t, F_{end} is the fluorescence intensity at maximum recovery, F_{start} is the fluorescence

17

441   recovery momentarily after bleaching (at t = 0), and k is a free parameter. The recovery

442   half-time was then extracted from $t_{1/2}$ = ln 2 / k. Importantly, all cells were scanned

443   from top to bottom in order to find the division plane (in which the rings reside).

444

445   *Image analysis*

446   Image analysis was performed using Fiji. When necessary, images were background-

447   corrected using a rolling ball with radius 36. Image stacks were motion-corrected using

448   the plug-in StackReg. Kymographs were generated from time-lapse images using the

449   KymoResliceWide plugin (line width 5), from which treadmilling speeds were

450   calculated using the slope of the fluorescence trace, as previously described [38].

451   STED images were deconvolved using Huygens Professional deconvolution software

452   (SVI, the Netherlands). FtsZ-ring diameters were extracted from the average values

453   of the Gaussian fitted fluorescence profiles drawn from 12 - 6 o'clock and 3 - 9 o'clock.

454   Side lengths of shaped cells were determined by applying line profiles in ImageJ. The

455   lengths and widths of individual FtsZ densities were obtained using line scans (line

456   size 4) over at least 5 randomly selected individual fluorescence spots from each

457   deconvolved cell image, whereby a Gaussian was fitted to the intensity profiles in order

458   to extract the Full Width at Half Maximum (FWHM). Note that the long and short axes

459   of each individual FtsZ density were assigned as "length" and "width", respectively,

460   regardless of orientation relative to the membrane. FtsZ cluster dimensions are given

461   in mean $\pm$ S.D. n indicates number of cells, unless explicitly specified.

462

463   *Statistical analysis*

464   Boxes represent S.D., with red lines indicating mean. Whiskers on the box plots

465   encompass 95.5% of the distribution. For statistical analyses, two-tailed Student's *t*-

466   tests were performed using Origin Pro 9. A *p*-value of < 0.05 was considered as

467   statistically significant.

468

469   *Data availability*

470   Data presented and material used in this paper can be available upon request from

471   the authors.

472

473   **Acknowledgements**

474   The authors would like to thank Harold Erickson (Duke Uni.) for sharing the FtsZ-

475   mNeonGreen strain. Daniel Daley (Stockholm Uni.) is acknowledged for valuable

476   suggestions to improve the manuscript. BS is supported by JSPS KAKENH (grant

477   number JP17K15694). Work in the SCB unit at OIST is funded by core subsidy from

478   Okinawa Institute of Science and Technology Graduate University.

479

480   **Author contributions**

481   B.S. conceived the study and performed the experiments. A.B. and B.S. designed and

482   engineered the micron pillar arrays. H.C. contributed reagents. B.S. and U.S. analyzed

483   the data. B.S. wrote the manuscript with input from all authors.

484

485   **Competing financial interests**

486   The authors declare no conflicting or competing financial interests.

487

488

References

490   1   de Boer, P. A. Advances in understanding *E. coli* cell fission. *Curr Opin*
491   *Microbiol* **13**, 730-737, doi:10.1016/j.mib.2010.09.015 (2010).

492   2   Lutkenhaus, J., Pichoff, S. & Du, S. Bacterial cytokinesis: From Z ring to
493   divisome. *Cytoskeleton* **69**, 778-790, doi:10.1002/cm.21054 (2012).

494   3   Meier, E. L. & Goley, E. D. Form and function of the bacterial cytokinetic ring.
495   *Current opinion in cell biology* **26**, 19-27, doi:10.1016/j.ceb.2013.08.006
496   (2014).

497   4   Haeusser, D. P. & Margolin, W. Splitsville: structural and functional insights
498   into the dynamic bacterial Z ring. *Nat Rev Microbiol* **14**, 305-319,
499   doi:10.1038/nrmicro.2016.26 (2016).

500   5   den Blaauwen, T., Hamoen, L. W. & Levin, P. A. The divisome at 25: the road
501   ahead. *Curr Opin Microbiol* **36**, 85-94, doi:10.1016/j.mib.2017.01.007 (2017).

502   6   Erickson, H. P., Anderson, D. E. & Osawa, M. FtsZ in bacterial cytokinesis:
503   cytoskeleton and force generator all in one. *Microbiol Mol Biol Rev* **74**, 504-
504   528, doi:10.1128/MMBR.00021-10 (2010).

505   7   Ortiz, C., Natale, P., Cueto, L. & Vicente, M. The keepers of the ring:
506   regulators of FtsZ assembly. *FEMS microbiology reviews* **40**, 57-67,
507   doi:10.1093/femsre/fuv040 (2016).

508   8   Skoog, K., Söderström, B., Widengren, J., von Heijne, G. & Daley, D. O.
509   Sequential closure of the cytoplasm and then the periplasm during cell
510   division in *Escherichia coli*. *Journal of bacteriology* **194**, 584-586,
511   doi:10.1128/JB.06091-11 (2012).

512   9   Söderström, B. *et al.* Disassembly of the divisome in *Escherichia coli*:

513   evidence that FtsZ dissociates before compartmentalization. *Molecular*

514   *microbiology* **92**, 1-9, doi:10.1111/mmi.12534 (2014).

515   10   Egan, A. J. F. Bacterial outer membrane constriction. *Molecular microbiology*

516   **107**, 676-687, doi:10.1111/mmi.13908 (2018).

517   11   Fu, G. *et al.* In vivo structure of the *E. coli* FtsZ-ring revealed by

518   photoactivated localization microscopy (PALM). *PLoS One* **5**, e12682,

519   doi:10.1371/journal.pone.0012680 (2010).

520   12   Coltharp, C., Buss, J., Plumer, T. M. & Xiao, J. Defining the rate-limiting

521   processes of bacterial cytokinesis. *Proc Natl Acad Sci U S A* **113**, E1044-

522   1053, doi:10.1073/pnas.1514296113 (2016).

523   13   Yang, X. *et al.* GTPase activity-coupled treadmilling of the bacterial tubulin

524   FtsZ organizes septal cell wall synthesis. *Science* **355**, 744-747,

525   doi:10.1126/science.aak9995 (2017).

526   14   Söderström, B., Chan, H., Shilling, P. J., Skoglund, U. & Daley, D. O. Spatial

527   separation of FtsZ and FtsN during cell division. *Molecular microbiology* **107**,

528   387-401, doi:10.1111/mmi.13888 (2018).

529   15   Bisson-Filho, A. W. *et al.* Treadmilling by FtsZ filaments drives peptidoglycan

530   synthesis and bacterial cell division. *Science* **355**, 739-743,

531   doi:10.1126/science.aak9973 (2017).

532   16   Schoenemann, K. M. & Margolin, W. Bacterial Division: FtsZ Treadmills to

533   Build a Beautiful Wall. *Curr Biol* **27**, R301-R303,

534   doi:10.1016/j.cub.2017.03.019 (2017).

21

535   17   Monteiro, J. M. *et al.* Peptidoglycan synthesis drives an FtsZ-treadmilling-

536   independent step of cytokinesis. *Nature* **554**, 528-532,

537   doi:10.1038/nature25506 (2018).

538   18   Moore, D. A., Whatley, Z. N., Joshi, C. P., Osawa, M. & Erickson, H. P.

539   Probing for Binding Regions of the FtsZ Protein Surface through Site-Directed

540   Insertions: Discovery of Fully Functional FtsZ-Fluorescent Proteins. *Journal of*

541   *bacteriology* **199**, doi:UNSP e00553 10.1128/JB.00553-16 (2017).

542   19   Wu, F., van Schie, B. G., Keymer, J. E. & Dekker, C. Symmetry and scale

543   orient Min protein patterns in shaped bacterial sculptures. *Nat Nanotechnol*

544   **10**, 719-726, doi:10.1038/nnano.2015.126 (2015).

545   20   Hussain, S. *et al.* MreB filaments align along greatest principal membrane

546   curvature to orient cell wall synthesis. *Elife* **7**, doi:10.7554/eLife.32471 (2018).

547   21   Garner, E. C. *et al.* Coupled, circumferential motions of the cell wall synthesis

548   machinery and MreB filaments in *B. subtilis*. *Science* **333**, 222-225,

549   doi:10.1126/science.1203285 (2011).

550   22   Weiss, D. S., Chen, J. C., Ghigo, J. M., Boyd, D. & Beckwith, J. Localization

551   of FtsI (PBP3) to the septal ring requires its membrane anchor, the Z ring,

552   FtsA, FtsQ, and FtsL. *Journal of bacteriology* **181**, 508-520 (1999).

553   23   Söderström, B. *et al.* Coordinated disassembly of the divisome complex in

554   *Escherichia coli*. *Molecular microbiology* **101**, 425-438,

555   doi:10.1111/mmi.13400 (2016).

556   24   Rowlett, V. W. & Margolin, W. 3D-SIM super-resolution of FtsZ and its

557   membrane tethers in *Escherichia coli* cells. *Biophysical journal* **107**, L17-20,

558   doi:10.1016/j.bpj.2014.08.024 (2014).

22

559   25   Anderson, D. E., Gueiros-Filho, F. J. & Erickson, H. P. Assembly dynamics of

560   FtsZ rings in *Bacillus subtilis* and *Escherichia coli* and effects of FtsZ-

561   regulating proteins. *Journal of bacteriology* **186**, 5775-5781,

562   doi:10.1128/JB.186.17.5775-5781.2004 (2004).

563   26   Young, K. D. The selective value of bacterial shape. *Microbiol Mol Biol Rev*

564   **70**, 660-703, doi:10.1128/MMBR.00001-06 (2006).

565   27   Mannik, J. *et al.* Robustness and accuracy of cell division in *Escherichia coli*

566   in diverse cell shapes. *Proceedings of the National Academy of Sciences of*

567   *the United States of America* **109**, 6957-6962, doi:10.1073/pnas.1120854109

568   (2012).

569   28   Mannik, J., Driessen, R., Galajda, P., Keymer, J. E. & Dekker, C. Bacterial

570   growth and motility in sub-micron constrictions. *Proceedings of the National*

571   *Academy of Sciences of the United States of America* **106**, 14861-14866,

572   doi:10.1073/pnas.0907542106 (2009).

573   29   Zhou, Z. *et al.* The contractile ring coordinates curvature-dependent septum

574   assembly during fission yeast cytokinesis. *Mol Biol Cell* **26**, 78-90,

575   doi:10.1091/mbc.E14-10-1441 (2015).

576   30   Minc, N., Burgess, D. & Chang, F. Influence of cell geometry on division-plane

577   positioning. *Cell* **144**, 414-426, doi:10.1016/j.cell.2011.01.016 (2011).

578   31   Takeuchi, S., DiLuzio, W. R., Weibel, D. B. & Whitesides, G. M. Controlling

579   the shape of filamentous cells of *Escherichia coli*. *Nano Lett* **5**, 1819-1823,

580   doi:10.1021/nl0507360 (2005).

581   32   Wong, F. *et al.* Mechanical strain sensing implicated in cell shape recovery in

582   *Escherichia coli*. *Nat Microbiol* **2**, 17115, doi:10.1038/nmicrobiol.2017.115

583   (2017).

584   33   Monahan, L. G. *et al.* Rapid conversion of *Pseudomonas aeruginosa* to a

585   spherical cell morphotype facilitates tolerance to carbapenems and penicillins

586   but increases susceptibility to antimicrobial peptides. *Antimicrobial agents and*

587   *chemotherapy* **58**, 1956-1962, doi:10.1128/AAC.01901-13 (2014).

588   34   Yao, Q. *et al.* Short FtsZ filaments can drive asymmetric cell envelope

589   constriction at the onset of bacterial cytokinesis. *EMBO J*,

590   doi:10.15252/embj.201696235 (2017).

591   35   Strauss, M. P. *et al.* 3D-SIM Super Resolution Microscopy Reveals a Bead-

592   Like Arrangement for FtsZ and the Division Machinery: Implications for

593   Triggering Cytokinesis. *PLoS biology* **10**, doi:ARTN e1001389

594   10.1371/journal.pbio.1001389 (2012).

595   36   Holden, S. J. *et al.* High throughput 3D super-resolution microscopy reveals

596   *Caulobacter crescentus* in vivo Z-ring organization. *Proceedings of the*

597   *National Academy of Sciences of the United States of America* **111**, 4566-

598   4571, doi:10.1073/pnas.1313368111 (2014).

599   37   Jacq, M. *et al.* Remodeling of the Z-Ring Nanostructure during the

600   *Streptococcus pneumoniae* Cell Cycle Revealed by Photoactivated

601   Localization Microscopy. *mBio* **6**, doi:10.1128/mBio.01108-15 (2015).

602   38   Loose, M. & Mitchison, T. J. The bacterial cell division proteins FtsA and FtsZ

603   self-organize into dynamic cytoskeletal patterns. *Nature cell biology* **16**, 38-46,

604   doi:10.1038/ncb2885 (2014).

605   39   Stricker, J., Maddox, P., Salmon, E. D. & Erickson, H. P. Rapid assembly

606   dynamics of the *Escherichia coli* FtsZ-ring demonstrated by fluorescence

607   recovery after photobleaching. *Proceedings of the National Academy of*

608   *Sciences of the United States of America* **99**, 3171-3175,

609   doi:10.1073/pnas.052595099 (2002).

610   40   Surovtsev, I. V. & Jacobs-Wagner, C. Subcellular Organization: A Critical

611   Feature of Bacterial Cell Replication. *Cell* **172**, 1271-1293,

612   doi:10.1016/j.cell.2018.01.014 (2018).

613   41   Caccamo, P. D. & Brun, Y. V. The Molecular Basis of Noncanonical Bacterial

614   Morphology. *Trends Microbiol* **26**, 191-208, doi:10.1016/j.tim.2017.09.012

615   (2018).

616   42   Gibson, D. G. *et al.* Enzymatic assembly of DNA molecules up to several

617   hundred kilobases. *Nature methods* **6**, 343-U341, doi:10.1038/NMETH.1318

618   (2009).

619   43   Amann, E., Ochs, B. & Abel, K. J. Tightly regulated tac promoter vectors

620   useful for the expression of unfused and fused proteins in *Escherichia coli.*

621   *Gene* **69**, 301-315 (1988).

622   44   Antonov, P. V., Zuiddam, M. R. & Frenken, J. W. M. Fabrication of high-

623   aspect ratio silicon nanopillars for tribological experiments. *J Micro-Nanolith*

624   *Mem* **14**, doi:Artn 044506 10.1117/1.Jmm.14.4.044506 (2015).

625   45   Ayari-Kanoun, A., Aydinoglu, F., Cui, B. & Saffih, F. Silicon nanostructures

626   with very large negatively tapered profile by inductively coupled plasma-RIE. *J*

627   *Vac Sci Technol B* **34**, doi:Artn 06kd01 10.1116/1.4964402 (2016).

628   46   Martin, M. *et al.* Fabrication of high-density Si and SixGe1-x nanowire arrays

629   based on the single step plasma etching process. *J Vac Sci Technol B* **31**,

630   doi:Artn 041806

631   10.1116/1.4812792 (2013).

632   47   Engstrom, D. S. & Soh, Y. A. Controlling the silicon nanowire tapering angle in

633   dense arrays of silicon nanowires using deep reactive ion etching. *J Vac Sci*

634   *Technol B* **31**, doi:Artn 021806 10.1116/1.4793500 (2013).
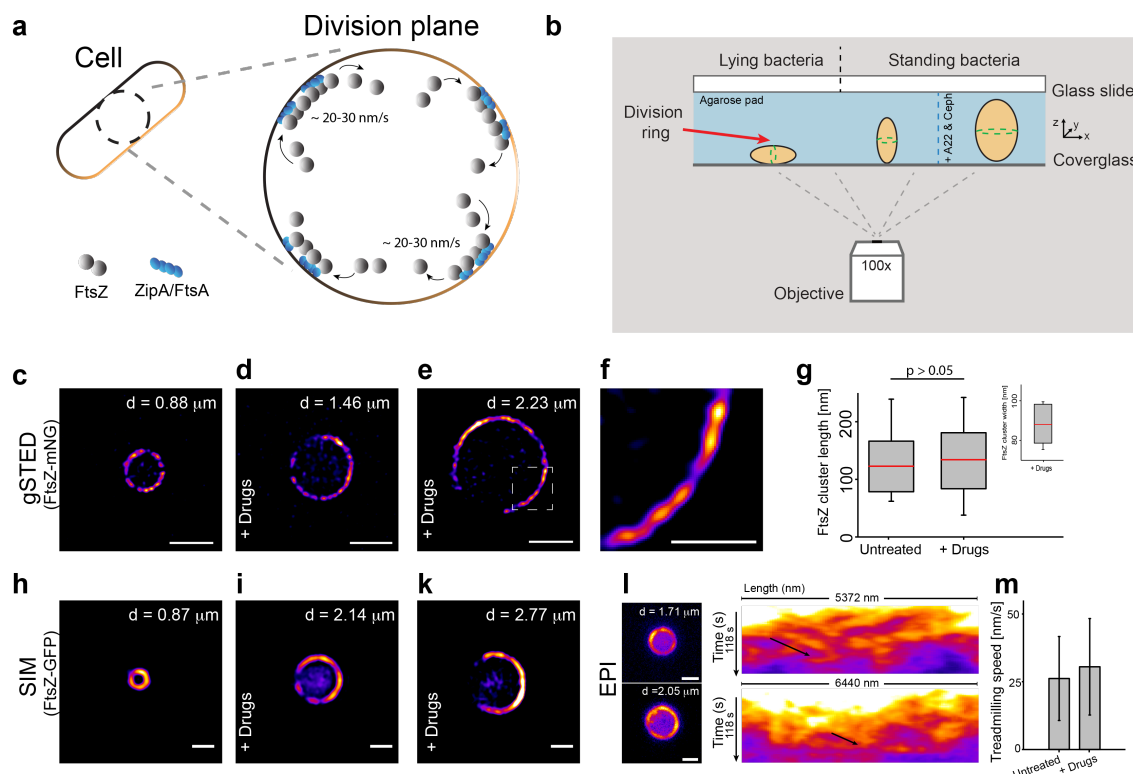
635

636

637

638

639

640

641   **Figures and Tables**

642

643

Figure 1. Midcell Z-ring assembly is unaffected by increased cell diameter.

645   **a**, Simplified cartoon showing FtsZ treadmilling at the division plane of an

646   *E. coli* cell. For clarity, only the membrane tethers, FtsA and ZipA, are shown.

647   **b**, Schematic representation of cell placement for imaging. Standing cells were

648   trapped in a vertical position in micron-sized holes in agarose pads created using

649   micron-sized pillars. Conditions for proper division ring placement are met when width

650   < length. The left and middle cells represent untreated cells. The cell on the right has

651   increased dimensions due to drug exposure (A22 and cephalexin). **c**, Time-gated

652   STED (gSTED) image of a typical FtsZ-ring (FtsZ-mNeonGreen) in an untreated

653   standing cell. Scale bar = 1 μm. **d** and **e**, gSTED images of FtsZ-mNeonGreen rings

654   in *E. coli* cells treated with drugs, showing increased ring diameter. Scale bar = 1 μm.

655   "Drugs" refer to A22 and cephalexin. **f**, Close-up of representative FtsZ densities

27

656   shown in **e**, from a cell with increased diameter. Scale bar = 0.5 μm. **g**, Quantification

657   of FtsZ density lengths in untreated and drug-treated cells. Mean $\pm$ S.D. was 122.8 $\pm$

658   43.9 nm (n = 77) and 132.4 $\pm$ 48.7 nm (n = 172) for untreated and drug-treated cells,

659   respectively. No statistically significant difference was measured, p > 0.05. Inset

660   shows density widths in drug-treated cells, mean $\pm$ S.D. = 88.4 $\pm$ 9.8 nm (n = 172). **h**

661   **- k**, Structured Illumination Microscopy (SIM) images of FtsZ-GFP in *E. coli* cells (**h**)

662   untreated or (**i** - **k**) treated with drugs. Scale bars = 1 μm. **l**, Snapshots of

663   epifluorescence (EPI) images from time-lapse series of FtsZ-GFP dynamics in drug-

664   treated cells. Scale bars = 1 μm. Corresponding kymographs are shown adjacent to

665   each image. Black arrows point to examples of FtsZ trajectories. **m**, Average

666   treadmilling speed of FtsZ-GFP in untreated (26 ± 15 nm/s, n = 102) and drug-treated

667   cells (30 ± 18 nm/s, n = 102). "d" in (**c** - **e**) and (**h** - **l**) indicates cell diameter.

668

669

670

671
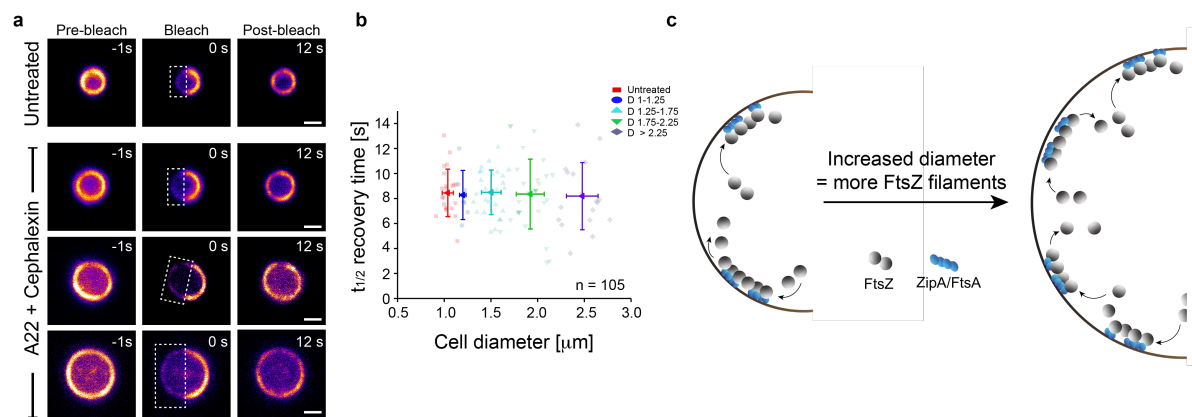
672

673

674

675

676

677

Figure 2. Cell size independent recovery of fluorescence in FtsZ-rings.

FRAP measurements on FtsZ-GFP rings in *E. coli* cells trapped standing in a vertical position. **a**, Representative cells of different diameter, untreated or treated with drugs. White boxes indicate bleached areas. Scale bars = 1 μm. **b**, Quantification of FRAP data from untreated cells (red), and drug-treated cells (other colors), showing that fluorescence recovery time is independent of cell diameter (in the range investigated, *i.e.* ~ 1 - 3 μm). n_{tot} = 105. "D" = cell diameter range. (see SI text for detailed values). **c**, Schematic representation of possible FtsZ filament distribution in cells of different diameters. Cells with larger diameter can accommodate a greater number of FtsZ filaments.

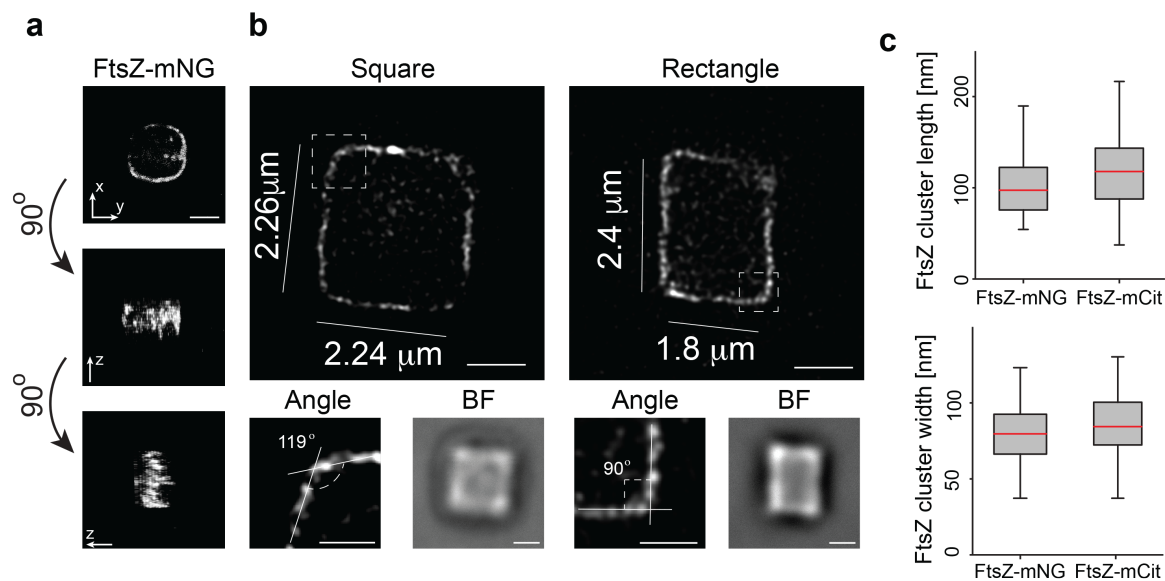**Figure 3. FtsZ-squares and -rectangles in shaped cells.**

Drug-treated (A22 and cephalexin) *E. coli* cells expressing FtsZ-mNeonGreen were sculptured into rectangular shapes and imaged using super-resolution STED nanoscopy. **a**, 3D rendering of a confocal Z-stack of an FtsZ-mNeonGreen square, showing only one band of FtsZ. Note that information along the z-axis is elongated. **b**, Representative STED images of FtsZ-mNeonGreen in square (left) and rectangular (right) cells with perimeters ranging from 8.4 to 11.52 μm (compared to WT ~ 3 μm). Additional examples are provided in Supplementary Fig. S9. Close-up images show representative corner angles. BF, brightfield image of corresponding cells. **c**, Quantification of FtsZ cluster dimensions, showing little difference between FtsZ-mNeonGreen (105.4 $\pm$ 39.6, 79.6 $\pm$ 18.2; length and width, respectively. n = 147) and FtsZ-mCitrine (118.3 $\pm$ 41.3, 86.3 $\pm$ 22.5; length and width, respectively. n = 162. Example images of FtsZ-mCitrine squares are shown in Supplementary Fig. S10). Scale bars = 1 μm.

30

712
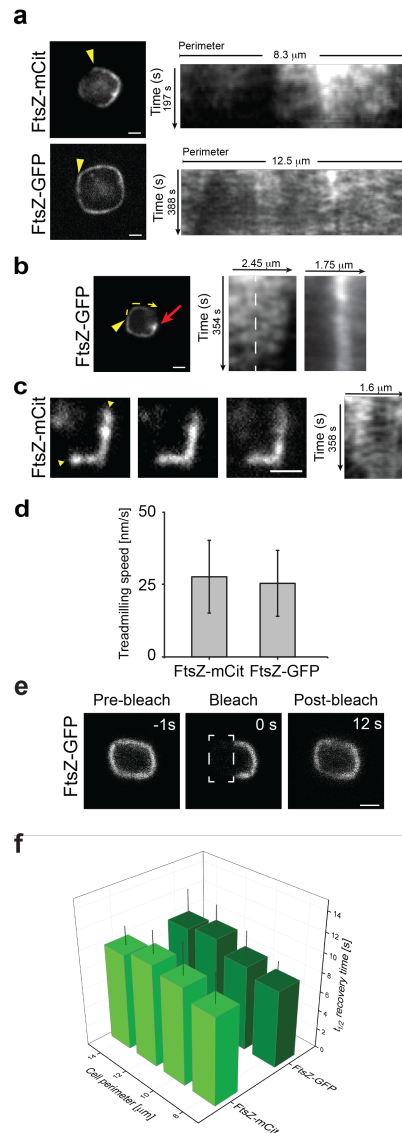
Figure 4. FtsZ dynamics in rectangular-shaped cells.

The dynamics of FtsZ in rectangular shapes were assessed by time-lapse imaging and FRAP measurements on *E. coli* cells expressing FtsZ-mCitrine or FtsZ-GFP. **a** - **c**, Snapshot images from time-lapse series of FtsZ-mCitrine or FtsZ-GFP in rectangular shaped cells. Corresponding kymographs are shown next to each image. **a**, Kymographs were taken around the entire perimeter (starting in the upper left corner, moving counter-clockwise, indicated by the yellow arrowheads). **b**, Kymographs were taken along the yellow line starting at the yellow arrowhead (left kymograph), or over the bright spot indicated by the red arrow (right kymograph). The

722   white striped line in **b** indicates the upper left corner of the cell. **c**, Kymograph taken

723   between the yellow arrowheads (top to bottom is left to right in the kymograph). **d**,

724   Average treadmilling speed of FtsZ-mCitrine and FtsZ-GFP in rectangles was $27.6 \pm$

725   12.5 nm/s (n = 97) and 25.3 ± 11.3 nm/s (n = 122), respectively. **e**, Typical FRAP

726   measurement of FtsZ-GFP in a rectangular *E. coli* cell. Half of the rectangle was

727   bleached. **f**, Average recovery times for FtsZ-mCitrine (light, n_{tot} = 24) and FtsZ-GFP

728   (dark, n_{tot} = 22) in FtsZ-rectangles of various perimeter lengths (see SI text for detailed

729   values). Scale bars = 1 μm.

730

731

732

733

734

735

736
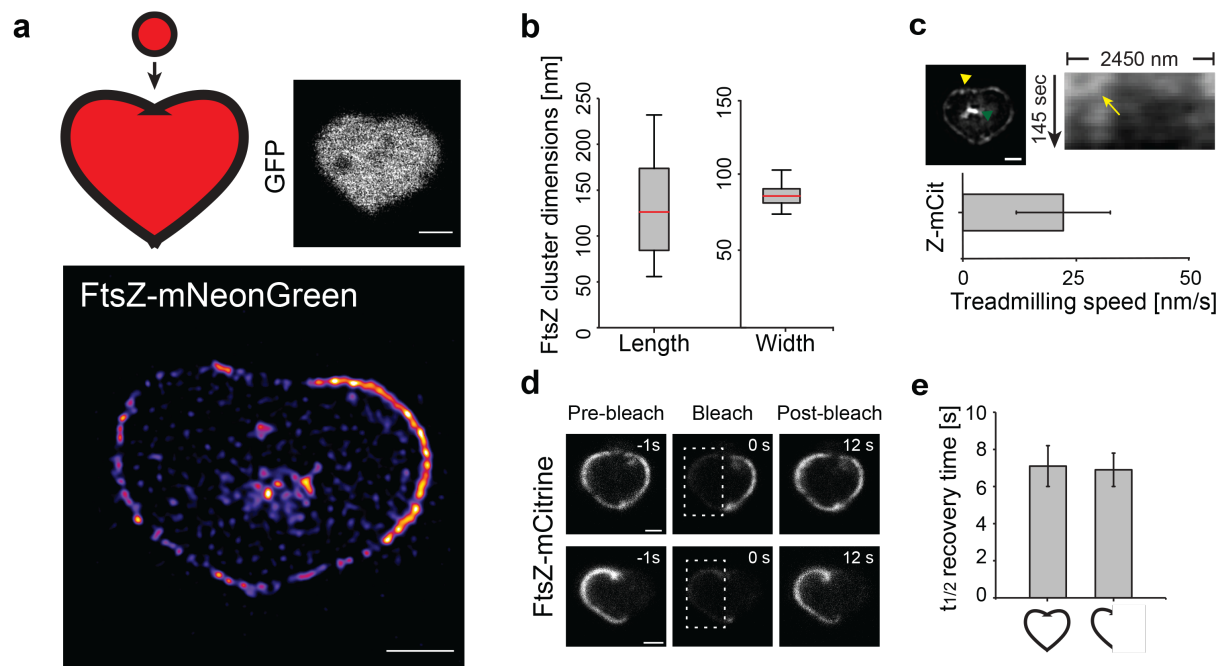
737

738

739

740

Figure 5. FtsZ cluster dimensions and dynamics in heart-shaped cells.

FtsZ behavior in *E. coli* cells sculptured into heart shapes. **a**, Upper left, Cartoon representation of a WT *E. coli* cell and a heart shape, highlighting the large and complex structural changes of a cell-to-heart transition, approximately to scale. Upper right, Drug-treated cell expressing cytoplasmic GFP, shaped as a heart. Lower, STED image of an "FtsZ-heart" (FtsZ-mNeonGreen) in a drug-treated *E. coli* cell. **b**, Lengths and widths of 155 individual FtsZ-mNeonGreen fluorescence densities in cells shaped as hearts. Average length = 129 ± 44 nm and width = 84 ± 9 nm. **c**, Upper row, SIM image from a time-lapse series (epi-fluorescence) of a heart-shaped cell expressing FtsZ-mCitrine. Green arrowhead indicates internal FtsZ clustering. Corresponding kymograph is shown adjacent to the image, and was generated starting at the yellow arrowhead in the SIM image, moving counter-clockwise for the indicated length. The yellow arrow points to an FtsZ trajectory. Lower, average treadmilling speed of FtsZ-mCitrine (Z-mCit) filaments in hearts (22.6 ± 10.4 nm/s, n = 44). **d**, FRAP measurements of FtsZ-mCitrine in heart-shaped cells. Top row, bleaching of half the FtsZ-mCitrine molecules in a 'full' heart. Bottom row, bleaching of a 'half-full' heart. No

33

758   difference in recovery time was observed. **e**, Histogram of average $t_{1/2}$ recovery times

759   calculated from FRAP measurements. Recovery in 'full hearts': 7.1 ± 1.1 s (n = 24),

760   recovery in 'half hearts': 6.9 ± 0.9 s (n = 9).

761

762

763

764

765

766

767
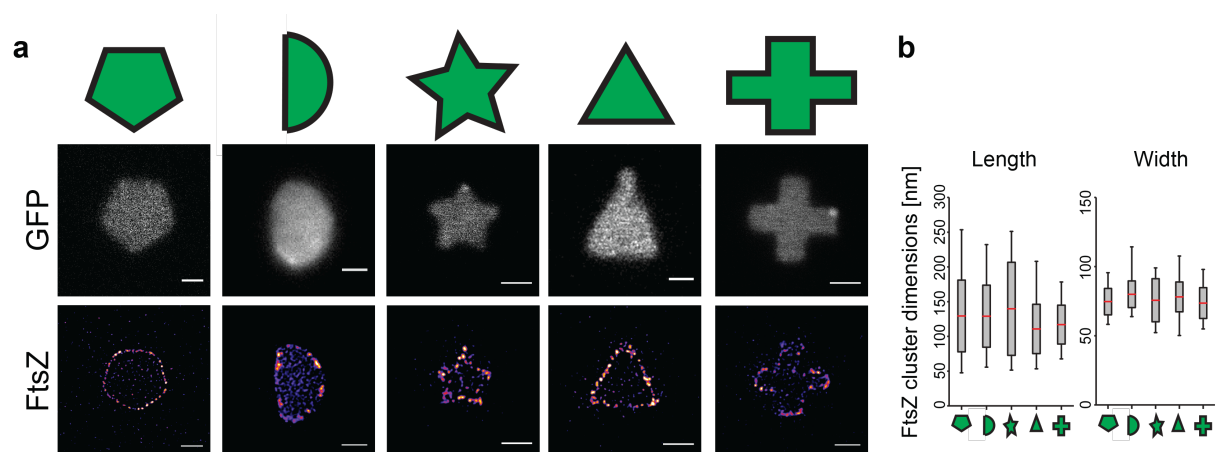
768

769

770

771

772

773

774

775

776

777

778

779

780

781

782

783

784

785

Figure 6. FtsZ bundle dimensions in complex shapes.

a, Cells expressing cytosolic GFP or FtsZ-mCitrine were remodeled into various shapes. Top row, schematic representation of the cell shapes. Middle row, representative cells expressing cytosolic GFP, and sculptured in the corresponding shapes. Bottom row, an FtsZ-pentagon, FtsZ-half-moon, FtsZ-star, FtsZ-triangle and FtsZ-cross in sculptured cells. Scale bars = 1 μm. **b**, Quantification of FtsZ densities by length and width in shaped cells (see SI text for detailed values).

793

FtsZ density dimensions

Cell shape	FP[*]	Drugs[$]	Length [nm]	Width [nm]
◯ (WT)	mNG	−	123 ± 44	80 ± 2
◯	mNG	+	132 ± 48	88 ± 9
▢	mNG	+	105 ± 40	80 ± 18
▢	mCit	+	118 ± 41	86 ± 22
♡	mNG	+	129 ± 44	84 ± 9
⬠	mNG	+	131 ± 52	74 ± 9
◗	mNG	+	129 ± 45	80 ± 10
☆	mNG	+	140 ± 67	76 ± 16
△	mNG	+	110 ± 35	78 ± 11
✚	mNG	+	119 ± 21	71 ± 18

* Fluorescent protein; mNG = mNeonGreen, mCit = mCitrine
$ Drugs; A22 [16 μM] and Cephalexin [20 μM]

794
795

796 **Table 1. Summary of FtsZ density dimensions at midcell in various cell**

797 **shapes.** In all cell shapes, the average measured density lengths were within 17 %

798 of WT, while average widths were within 13 %. Numbers represent mean ± S.D.

799 Note that values are rounded to whole integers.

800

801

802

803

804

FtsZ Dynamics

Cell shape	FP[*]	Drugs[$]	Treadmilling speed [nm/s]	$t_{1/2}$ recovery [s]
◯ (WT)	GFP	—	26 ± 15	8 ± 2
◯	GFP	+	30 ± 18	8 ± 2
▢	mCit	+	28 ± 13	10 ± 3
▢	GFP	+	25 ± 11	9 ± 3
♡	mCit	+	23 ± 10	7 ± 1

* Fluorescent protein; mCit = mCitrine $ Drugs; A22 [16 μM] and Cephalexin [20 μM]

805

806

807   **Table 2. Summary of FtsZ dynamics in various cell shapes.**

808   Numbers represent mean ± S.D. Note that values are rounded to whole integers.

809